

ZnO tetrapod morphology influence on UV sensing properties

Mindaugas Ilickas¹ , Rasa Mardosaite^{1,2}, Federico Cesano³ ,
Sara Cravanzola³ , Claudia Barolo³, Domenica Scarano³ ,
Guido Viscardi³  and Simas Rackauskas^{1,2} 

¹Institute of Materials Science, Kaunas University of Technology, K. Barsausko St. 59, 51423 Kaunas, Lithuania

²Department of Physics, Kaunas University of Technology, Studentu St. 50, 51368 Kaunas, Lithuania

³Department of Chemistry, NIS Interdepartmental Centre and INSTM Reference Centre, University of Turin, Via Pietro Giuria 7, I-10125 Turin, Italy

E-mail: simas.rackauskas@ktu.lt

Received 28 April 2023, revised 17 August 2023

Accepted for publication 24 September 2023

Published 19 October 2023



CrossMark

Abstract

The aim of this work was to investigate how ZnO tetrapod (ZnO-T) morphology, structure, and surface charge properties (i.e. Debye length) influence their UV sensing properties, shedding light on the underlying photoresponse mechanisms. ZnO-Ts were synthesized and centrifuged to obtain three different fractions with tuned morphology, which were characterized by scanning electron microscopy, transmission electron microscopy, and high-resolution transmission electron microscopy microscopies, x-ray diffraction analysis, Brunauer–Emmett–Teller measurements, FTIR and UV–vis spectroscopies. ZnO-T UV sensors were fabricated and tested comparing among ZnO-T fractions and commercial ZnO nanoparticles. ZnO-T photoresponse was mostly influenced by ZnO-T leg diameter, with the optimal value close to the double Debye length. We also demonstrated how fractionating ZnO-Ts for morphology optimization can increase the responsivity by 2 orders of magnitude. Moreover, ZnO-T showed 3 orders of magnitude higher responsivity compared to commercial ZnO nanopowder. These results are beneficial for the engineering of efficient UV sensors and contribute to a deeper understanding the overall mechanism governing UV photoresponse.


Keywords: ZnO tetrapods, UV sensing, porosity measurements, Debye length, chemoresistive, FTIR spectroscopy

(Some figures may appear in colour only in the online journal)

1. Introduction

The control over the crystal sizes and shapes of nanostructured materials has attracted growing interest due to the possibility of a feasible control of properties [1–3]. Lowering the dimensions of nanostructure increases the fraction of atoms, located at the surface, resulting in special surface-related properties conferred by boundaries, edges, corners,

steps and other arrangements [4, 5]. Abundant examples of known materials with a low-dimensional character, include oxides, nitrides, transition-metal dichalcogenides [6, 7], pure elements (i.e. Xenon), polymers [8–10] and carbon-based materials (i.e. graphene type, and 2D amorphous carbons) [11–13]. Among the oxides, ZnO is of particular interest due to its abundance and resulting in a variety of structures. Low-dimensional ZnO crystals can be obtained in the form of small nanoparticles (0D), rod-like structure (1D), nanosheets (2D), and hybrid structures [14–18]. A peculiar morphology is characterized by four ZnO nanorods joining the central core, known as ZnO tetrapod structure [19, 20], exhibits various advanced properties, including optical, electronic, and

 Original content from this work may be used under the terms of the [Creative Commons Attribution 4.0 licence](https://creativecommons.org/licenses/by/4.0/). Any further distribution of this work must maintain attribution to the author(s) and the title of the work, journal citation and DOI.

piezoelectric ones [20]. Hence, ZnO tetrapods find wide-range applications in electronics and optoelectronics, including devices and sensors, transistors, ultraviolet/blue LEDs, field-emission displays, gas sensors and UV detectors, transparent conductive films, and hybrid solar cells [21–23]. However, it is still possible to further enhance the specific surface related properties by controlling the morphology parameters, such as rod lengths, basal sizes, length-to-diameter ratio, angles between arms, etc.

UV detectors are a key component in various applications such as UV imaging, flame detection, and air quality monitoring. Silicon-based photodetectors and photo-multipliers are commonly used as UV detectors due to their high sensitivity, low noise, and fast response in the UV region, however, these detectors have significant limitations, such as the need for filters to block low-energy photons, degradation, lower efficiency, and high voltage supply requirements [24]. Wide bandgap semiconductors, such as ZnO, have emerged as a promising alternative for UV detection due to their intrinsic visible-blindness and chemical and thermal stability, making them suitable for harsh environments [25]. Various types of ZnO-based photodetectors have been developed, including photoconductors, Schottky photodiodes, metal–semiconductor–metal photodiodes, and p–n junction photodetectors. By means of nanomaterials and using the chemoresistive principle, the morphology of ZnO-based UV photodetectors can be tuned to optimize their performance, thus resulting in high responsivity, high UV/visible contrast ratio, fast response time, and low noise characteristics [25].

Nanowires [26], in particular, show a high surface-to-volume ratio that provides a way to enhance the effects of surface phenomena (that are at the base of chemical sensing mechanism); moreover, they may be single crystalline and have well-defined crystal orientations [27], leading to controlled reactions and increased stability. Response dynamics should be faster compared to their polycrystalline [28] counterpart because there is no need for gas diffusion [29] preliminary to surface reaction. Finally, some of the interesting effects that can be exploited in chemical sensing (such as self-heating) exist only for the nanowire morphology [18]. ZnO-Ts morphology consists in a structure of 4 connected nanowires possessing an intrinsic porosity due to its packing structure, hence it is especially interesting for UV photodetector application, however more research on the methods for photoresponse tailoring is needed.

In this work, ZnO-Ts were synthesized and separated by centrifugal force into fractions with different sizes, which show different UV photoresponse. A thorough investigation of the fractions of ZnO-T structure and morphology was conducted by scanning and high-resolution transmission electron microscopy (SEM, HR-TEM), x-ray diffraction (XRD), surface area and porosity, Fourier-transform infrared spectroscopy (FTIR) and UV–vis spectroscopies. The study of CO probing the surface of ZnO-Ts at low temperature, provides precise surface information, which is correlated with the UV sensing. We discuss the influence of ZnO morphology, i.e. facet orientation, porosity, and leg diameter,

providing insights into the nature of the photoresponse properties of the ZnO nanostructures.

2. Materials and methods

2.1. Material preparation

ZnO-Ts were synthesized by means of a vapor-phase oxidation of Zn powders similarly to a before reported process [13]. Briefly, micron sized Zn powders (VWR Chemicals $\geq 97\%$ purity, particle size $\sim 5 \mu\text{m}$) were oxidized at 800°C in air atmosphere, inside a reactor, which consists of a vertical furnace, a powder feeder, and a system of products collection. Zn powder was continuously supplied into the vertical furnace using a powder feeder. Air was sucked at the top of the reactor from the surrounding atmosphere, and the vacuum was adjusted to the flow rate of 2.0 l min^{-1} . The obtained ZnO-Ts were collected downstream of the reactor on a nitrocellulose filter, $0.4 \mu\text{m}$ pore size, and then used without additional heat treatment.

ZnO-Ts were separated into fractions by size using centrifugal force. ZnO-T were first dispersed in absolute ethanol, sonicated for 10 min, 5 min settled, then the upper liquid part was centrifuged from 1000 to 3000 rpm. After centrifugation the floating part was used for characterization and sensor preparation.

Commercial ZnO powder named Kadox 25 was utilized for the comparison of the ZnO-T photoresponse properties.

2.2. Characterization techniques

The sample morphology was investigated by means of a Zeiss Evo50 SEM equipped with an Oxford energy dispersive x-ray detector, while the structure of the sample was obtained by a JEOL 3010-UHR TEM instrument operating at 300 kV, equipped with a $2\text{k} \times 2\text{k}$ pixels Gatan US1000 CCD camera.

The sample crystallinity and the mean crystallite sizes were estimated by a PANalytical X'Pert PRO XRD diffractometer, equipped with a Ni filtered Cu radiation in a standard Bragg–Brentano geometry. The identification of the phases was made by comparing XRD patterns with the powder diffraction file (PDF) reference of the International Centre for Diffraction Data (ICDD) database. The crystallite sizes were calculated from XRD measurements by Scherrer's equation.

N_2 adsorption–desorption experiments were carried out at 77 K on a Micromeritics ASAP 2020 instrument to determine the Brunauer–Emmett–Teller (BET) surface area and the porosity properties. Samples were outgassed at 423 K for 6 h before analysis. Pore size distributions (PSDs) of the samples were derived from the N_2 -adsorption isotherm data by using a non-negative least squares fitting and applying the density functional theory (DFT) method (NLDFT model for pillared clay, cylinder pore geometry) and from the Barret–Joyner–Halenda (BJH) model (Harkins–Jura with Faas correction).

FTIR measurements were obtained by means of a Bruker IFS-28 spectrometer equipped with a MCT detector. The FTIR

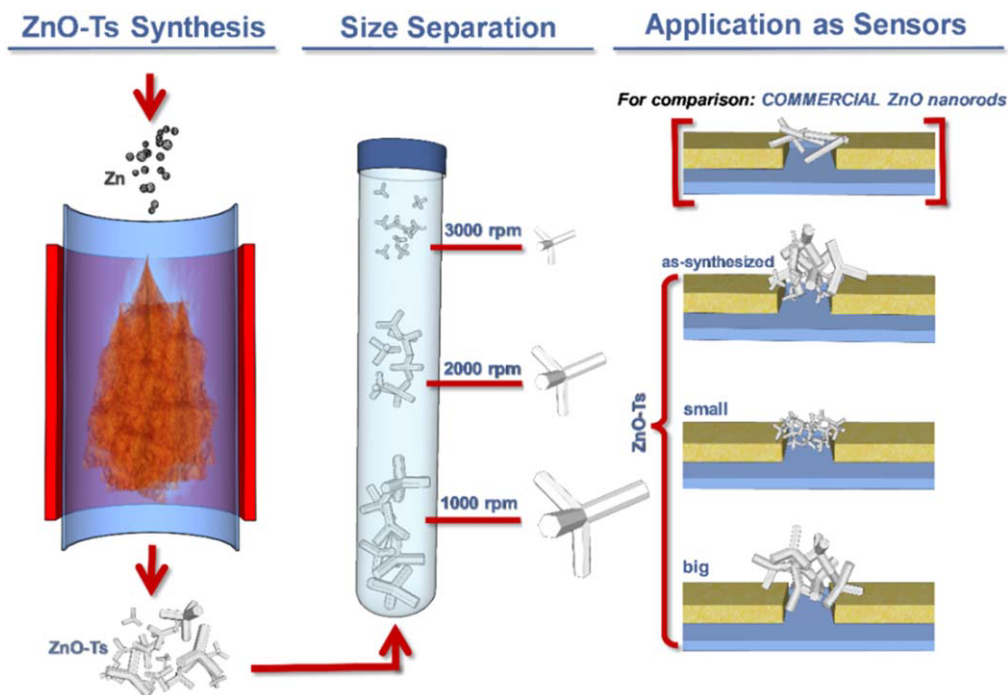


Figure 1. Scheme of ZnO-Ts synthesis for UV sensing application.

spectra of CO adsorbed at 100 K on ZnO samples, compressed in the form of pellets, were obtained with a resolution of 4 cm^{-1} (64 averaged interferograms for each spectrum) at decreasing CO coverages in an IR cell designed for liquid nitrogen flowing. Before CO dosage, the pellet, inside the IR cell, was outgassed for 1 h at 773 K under vacuum (10^{-5} torr), to clean the surface from adsorbed impurities and then heated in O_2 (10 torr) at the same temperature for 10 min. The treatment under O_2 was repeated three times to obtain a stoichiometric sample. At the end of the last oxidation cycle, the sample was cooled in O_2 at 298 K and then evacuated at the same temperature (final pressure 10^{-5} torr).

The optical properties of the ZnO-Ts were investigated at room temperature by using a double-beam UV–vis spectrophotometer (Varian Cary UV 300 Bio) operating in the wavelength range of 190–800 nm. The samples were dispersed in ethanol and the spectra of the solutions were recorded in the transmission mode.

UV sensors were made on opaque alumina ceramic substrate (VC 100-1 (Policor), 99.6%–99.9% Al_2O_3 , white, $\rho = 3.89\text{ g cm}^{-3}$, $R_a < 0.01\ \mu\text{m}$) between two Al electrodes preparing a $20\ \mu\text{m}$ wide trench by laser ablation. The electrodes after preparation were cleaned, sonicated and ZnO nanomaterial was deposited. To control the sensor size and exact placing, ZnO nanomaterials 1 mg ml^{-1} solution in ethanol was drop casted into $5 \times 5\text{ mm}$ plastic limiter on electrodes, controlling the deposited electrode resistivity, which was kept $100\text{ M}\Omega$ after drying for all samples. The UV response measurements were performed under atmospheric conditions in the presence (UV on) and absence of UV irradiation (UV off), using UV LED $\lambda = 365\text{ nm}$, $I = 0.31\text{ mW cm}^{-2}$. For green light illumination LED of $\lambda = 525\text{ nm}$, $I = 0.92\text{ mW cm}^{-2}$ was used.

3. Results and discussion

3.1. ZnO-Ts synthesis and effect of size separation

The different steps concerning the ZnO-Ts preparation together with the size separation and then the possible use as UV sensors is schematized in figure 1(a). After synthesis of ZnO-Ts from Zn nanoparticles, the as-obtained product was collected and fractioned by centrifugation. Centrifugal force is forcing larger particles to settle, leaving the suspension with only smaller ZnO-Ts, in such way, applying different centrifugal force leads to the separation of the particles into fractions by their dynamic size. The samples centrifuged at 1000 rpm, 2000 rpm and 3000 rpm were collected, dried at room temperature, and used for size-variant ZnO-Ts suspensions in ethanol. In earlier works the different ZnO-T fraction influence on optical [30] and electrochemical [21] properties were determined; however, the UV sensing properties were not tested. To determine how ZnO-T size influences UV sensing properties, chemoresistive UV sensors were prepared, being ZnO-Ts used to form a contact bridge between electrodes (figure 1(a)). The suspension of commercial ZnO nanorods was used in parallel to compare the obtained results with ZnO-Ts.

3.2. Morphology and structure from SEM, HRTEM and XRD analyses

ZnO-Ts fractions, before and after centrifugation at 1000 rpm, 2000 rpm and 3000 rpm, are SEM imaged in figures 2(a)–(d), respectively. All images are shown at the same magnification for better comparing the different samples. At first, from SEM images (figures 2(a)–(d)), a dense network of ZnO packed

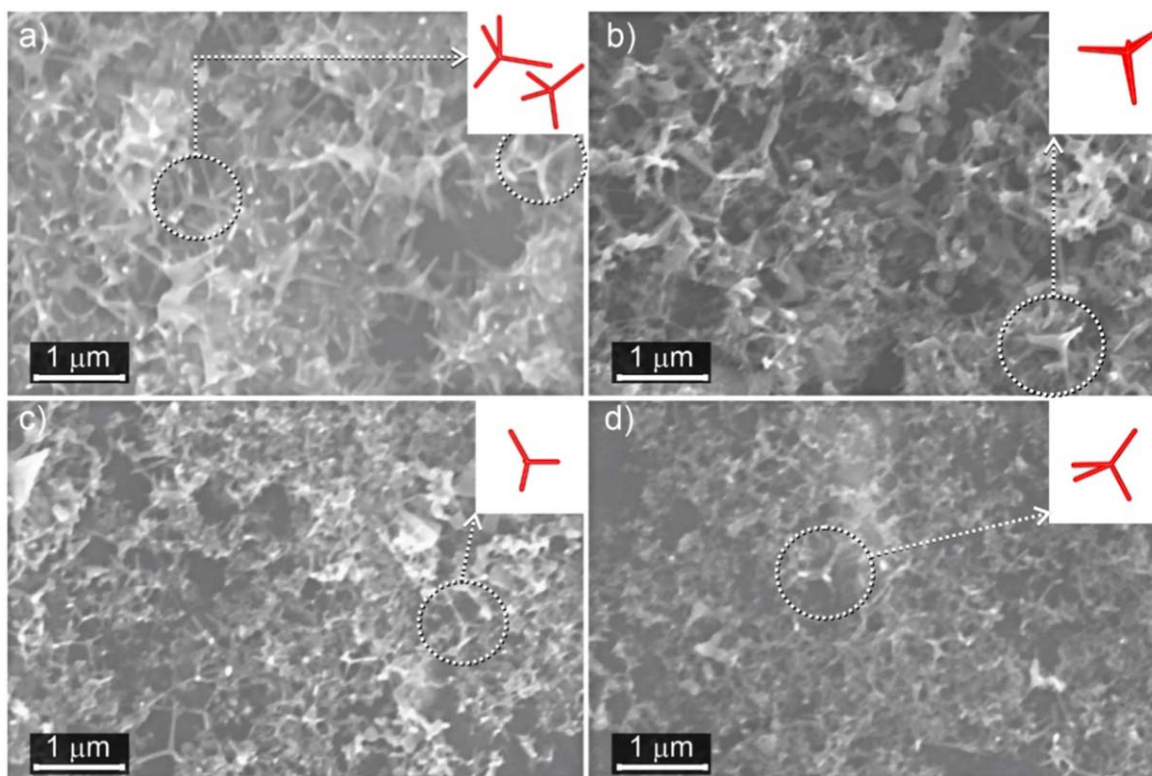


Figure 2. SEM images of ZnO-Ts before (a) and after centrifugation at: 1000 rpm (b); 2000 rpm (c); 3000 rpm (d). In the insets, models of the ZnO-T structures, corresponding to the selected areas of dotted circles in a, b, c, d figures, are schematized.

nanostructures composed of a few interconnected legs can be highlighted. Notice that, in the insets of figures 2(a)–(d), some models of the differently oriented tetrapods are illustrated. ZnO-Ts crystals have long legs made of prismatic faces 500–1000 nm range in length, while the basal planes are tens of nm in sizes, (*vide infra* from TEM images in figure 3 and inset).

However, also from SEM images (figures 2(a)–(d)), it comes that ZnO-Ts crystals after centrifugation become smaller both in basal (leg diameter) and prismatic (leg length) faces, although a clear evaluation of the relative sizes cannot be made. Conversely the evolution of the particle's sizes, due to the different centrifugation speeds can be clearly seen from TEM and HRTEM images in figures 3(a)–(d). It is noteworthy that, after synthesis, some particles ranging in 50–100 nm interval can also be observed together with ZnO-T crystals (figure 3(a), marked with white arrows). Interference fringes 0.28 nm spaced are found on the selected particle (figure 3(b)), which corresponds to the (10–10) interplanar distance of a ZnO Wurtzite structure. The selected electron diffraction area (SAED) (FFT image, top inset of figure 3(b)) on the dotted square region of the particle, shows a hexagonal crystal structure, which is compatible with the orientation along [0001] zone axis, which corresponds to the (0001) exposed face. From the IFFT-filtered image (bottom inset of figure 3(b)) of the same selected area, a lattice constant of 0.32 nm has been measured.

The constant increase of the full width at half maximum (FWHM) on patterns starting from as prepared ZnO-Ts

(black) to centrifuged at 3000 rpm (blue) can be followed in figure 4. It is well known that particle sizes can be calculated using the Scherrer method, in which the value of FWHM is inversely proportional to the crystallite's dimensions, represented by the coherent scattering domain size along the specific diffraction direction. It is also assumed that the peak broadening is primarily associated to the size of the crystalline domains, without significant contribution by other factors in affecting the peak broadening (and position), such as lattice strain, stacking faults, or microstrain effects.

From the obtained results, the decrease of the ZnO-Ts dimensions after centrifugation is proportional to increasing centrifugation rates, as shown in the inset of figure 4. In particular (100) and (002) diffraction peaks can be noticed (inset in figure 4), where the broadening of the FWHM is highlighted by the black arrows. Moving from as prepared ZnO-Ts, to ZnO-Ts centrifuged at 3000 rpm, the extension of the (100) and (002) domains are found to change from ~66 nm to 36 nm and from ~81 nm to 64 nm, respectively. The results obtained are reported in table 1.

3.3. Porosity and surface area from BET analysis

The N₂-adsorption/desorption isotherms obtained at 77 K and the related pore size distributions of the ZnO samples, are shown in figures 5(a) and (b), while BET surface area values, calculated from the adsorption branches, are summarized in table 2.

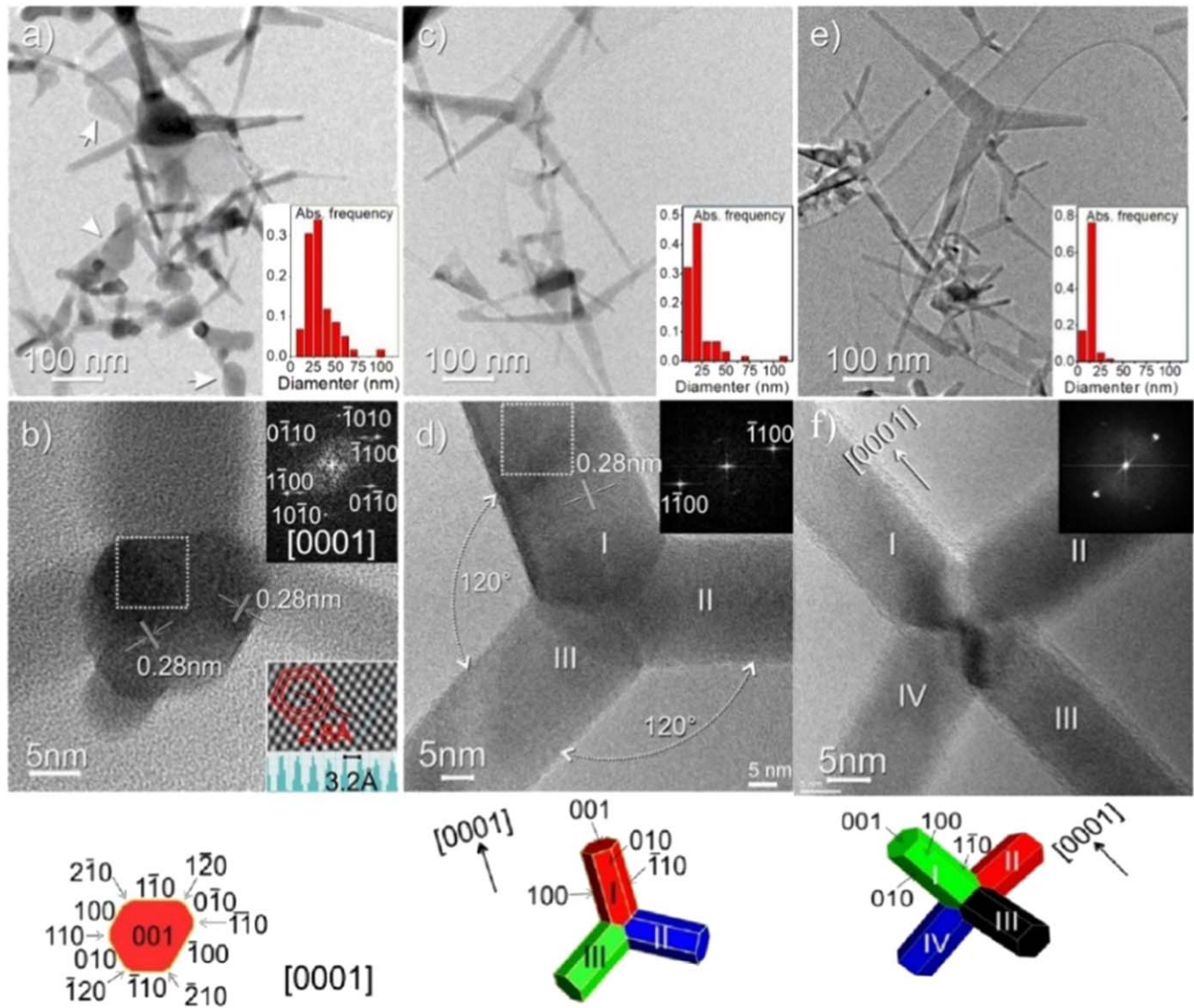


Figure 3. TEM and HRTEM images of ZnO-T crystals: as prepared (a), (b), after the centrifugation at 1000 rpm (c), (d) and 3000 rpm (e), (f). White arrows in (a) mark nanoparticles. Insets of a, c, e panels show the distributions of the ZnO-T leg diameters. The interplanar spacings along two directions on a selected area are shown in (b). Insets of (b): FFT image (top inset) and IFFT-filtered image (bottom inset) of the selected area by a dotted square of a ZnO particle. Inset of (d): FFT image of the selected area by a dotted square on a ZnO-T leg. The schematics at the bottom reproduce the shape and orientation of the ZnO-Ts imaged in (b), (d) and (f) and the assignment of their exposed surfaces.

All the isotherms could be categorized as type II, with minor hysteresis loops appearing in the $0.85 \leq p/p_0 \leq 1$ interval, thus indicating the presence of mesopores, which are conceivably generated by the nanocrystal shape and dimensions (figure 5(a)). The BET surface area of ZnO-Ts after thermal preparation was significantly higher than that of ZnO Kadox 25 powder (New Jersey Zinc Company) used as a reference powder material. Furthermore, from the comparison of BET surface area values of ZnO-Ts before and after centrifugation at 1000 rpm, 2000 rpm or 3000 rpm we can safely assume that the application of a centrifugal force is an effective procedure to progressively separate ZnO-Ts from the solution according to their size. The pore size distributions of the samples are reported in figure 5(b). From this figure, we can assume that all the tetrapod-based samples exhibit a

broader and extended mesoporosity, which becomes more restricted after the centrifugation steps with the presence of two main families of pores with sizes in the 20–40 Å range and >60 Å.

Therefore, the peculiar geometry of the tetrapods, which are connected together to form 3D spatially extended networks, prevents ZnO-Ts from achieving a highly effective close packing, thus causing a remarkable mesoporosity.

3.4. Surface and optical properties from FTIR and UV–visible spectra

Figure 6 shows the FTIR spectra of CO adsorbed at liquid nitrogen temperature on the surface of ZnO-Ts before (a) and after centrifugation at 1000 rpm (b) and at 3000 rpm (c),

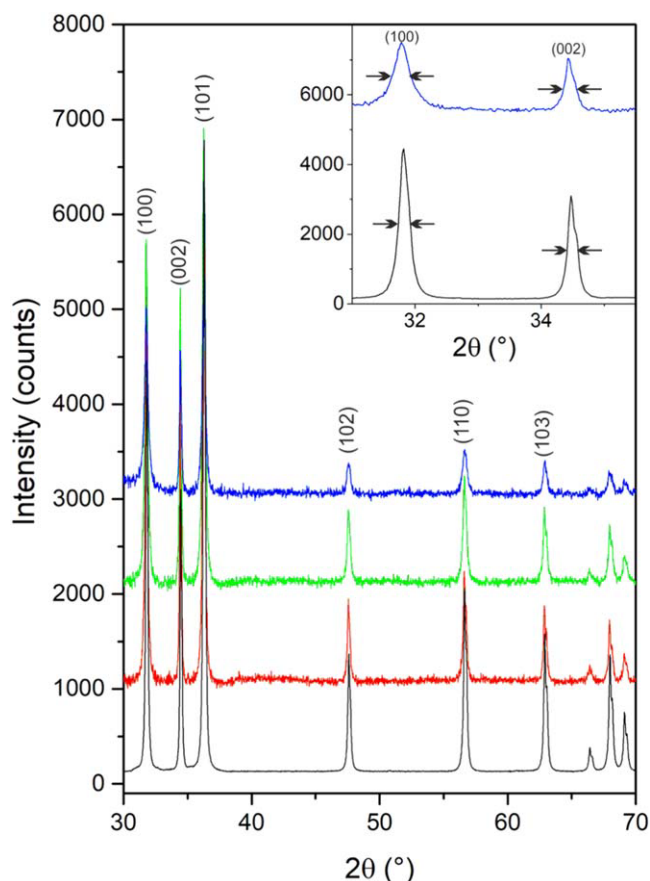


Figure 4. XRD patterns of as prepared ZnO-Ts (black pattern) and after centrifugation at 1000 rpm (red pattern), 2000 rpm (green pattern) and 3000 rpm (blue pattern). The inset shows an enlarged view of the (100) and (002) peaks of ZnO-Ts before centrifugation (black pattern) and after centrifugation at 3000 rpm (blue pattern), where the black arrows highlight the change in the FWHM value.

moving from high coverages ($\theta = 1$) (black lines) to progressively low coverages ($\theta = 0$) (grey lines).

At first, moving from the spectra of CO adsorbed on as prepared ZnO-Ts, (figures 6(a)–(a')) to those of CO on centrifuged samples (figures 6(b)–(b') and figures 6(c)–(c')), a general decreasing of all the features is observed, plausibly due to the centrifugation process, which causes the formation of small crystallites with less extended surfaces. Some more, envelopes in the 2220–2160 cm^{-1} range and in the 2160–2120 cm^{-1} range are observed, whose relative intensity is changing with the centrifugation conditions (figures 6(a), (a')–(c), (c')), which can be explained with a different contribution of the exposed surfaces (*vide infra*).

Hence the changes in the relative intensities of both the envelopes in the 2220–2160 cm^{-1} range and in the 2160–2120 cm^{-1} range are due to the progressively decreasing of the prismatic faces together with the increasing of the hydroxylated faces with a higher number of defects including steps, corners, and edges. In addition, the increased value of FWHM of the main band at 2168 cm^{-1} is a further indication that the size of the (10–10) and (11–20) prismatic surfaces have been decreased. This is fully confirmed by the previously discussed XRD, SEM and TEM results.

The main band in the 2190–2168 cm^{-1} range (figures 6(a)–(c)), due to CO on the Zn^{2+} ions on the (10–10) and (11–20) prismatic faces [15, 31], shifts from 2190 cm^{-1} ($\theta \rightarrow 0$) to 2168 cm^{-1} (maximum coverage, $\theta \rightarrow 1$), as a consequence of the building up of lateral interactions between the parallel CO oscillators, which are adsorbed on the ordered array of Zn^{2+} ions. Moreover, as θ changes from 0 to 1, the gradual decrease of the half-width of the band is observed, due to the progressive decrease of the disorder in the surface adlayer. At intermediate coverages, a few components in the 2170–2160 cm^{-1} range, whose intensity and frequency change gradually with θ (figures 6(a'), (b'), (c')), are due to the progressive stepwise filling of the surface Zn^{2+} sites, which corresponds to different variants of CO nearest neighbors. This behaviour is more visible on as prepared ZnO-Ts (figure 6(a')), however some change can be also evidenced on centrifuged samples (figures 6(b'), (c')).

Meanwhile, the shoulders at 2178 cm^{-1} and in the 2184–2180 cm^{-1} range in figures 6(b)–(c) are assigned to CO adsorbed on defective sites, like edges and corners of the main faces.

Notice that the bands in the 3750–3350 region (see the inset in figures 6(a)–(c)), which are associated to highly stable OH groups on defective sites of high index faces and defective sites, were not removed by the thermal treatment at 773 K in vacuum. Conversely, upon CO dosage, the bands are perturbed, being eroded and/or downshifted, because of the hydrogen interactions (see figure 7). Figure 8 shows the UV–vis spectra, acquired in the transmission mode, of the ZnO-Ts before and after centrifugations at increasing rates. The spectra reveal, a sharp absorption in the 400–600 nm interval due to the energy gap electron transitions, direct in type, from the valence band to the conduction band [32]. Moving from the black curve (as obtained ZnO-Ts) to the red, green, and then the blue ones (ZnO-Ts after increasing centrifugation rates), and then up to the green and blue curves (ZnO-Ts after), an upwards shift of the energy band gap is observed. This phenomenon can be ascribed to the decreased dimensions of the ZnO-Ts, which are collected from the supernatant fraction in the centrifuge tube. It is well known that the observed blue shift is explained by the quantum size effect [33, 34]. Moreover, larger particles tend to scatter light, therefore the slope to the maximum absorption becomes sharper with the decrease of ZnO-T size. The obtained results, concerning the evolution of the ZnO-Ts sizes, as a function of the centrifugation rate, have been also confirmed by SEM, TEM and XRD investigations, as shown in paragraph 3.2.

3.5. UV sensor performance

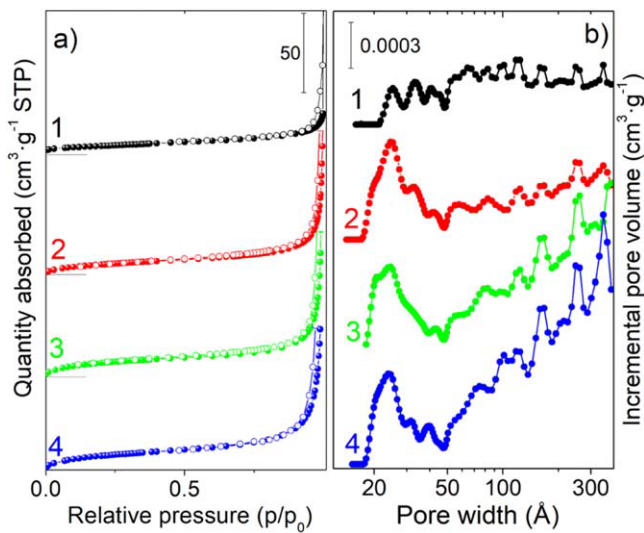
The UV sensing performance (figures 9(a)–(c)) was characterized as photoresponse to UV ($\lambda = 365 \text{ nm}$, $I = 0.31 \text{ mW cm}^{-2}$), where current–voltage (I – V) characteristics were obtained in the presence (UV on) and the absence of UV irradiation (UV off). The photoresponse mechanism of ZnO is characteristic to n-type semiconductor chemoresistive sensors in air [35]. The initial step involves the adsorption of

Table 1. Sizes of (100) and (002) scattering domains on ZnO-Ts as obtained from the Debye–Scherrer formula.

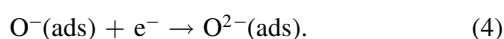
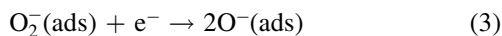
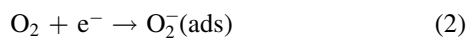
Samples	FWHM (°)	Dimensions (100)	Dimensions (002)
ZnO-Ts as prepared	0.18	66 nm	81 nm
ZnO-T centrifuged @1000 rpm	0.23	57 nm	80 nm
ZnO-T centrifuged @2000 rpm	0.27	45 nm	73 nm
ZnO-T centrifuged @3000 rpm	0.30	36 nm	64 nm

Table 2. Surface area ($\text{m}^2 \text{g}^{-1}$) of the ZnO-Ts.

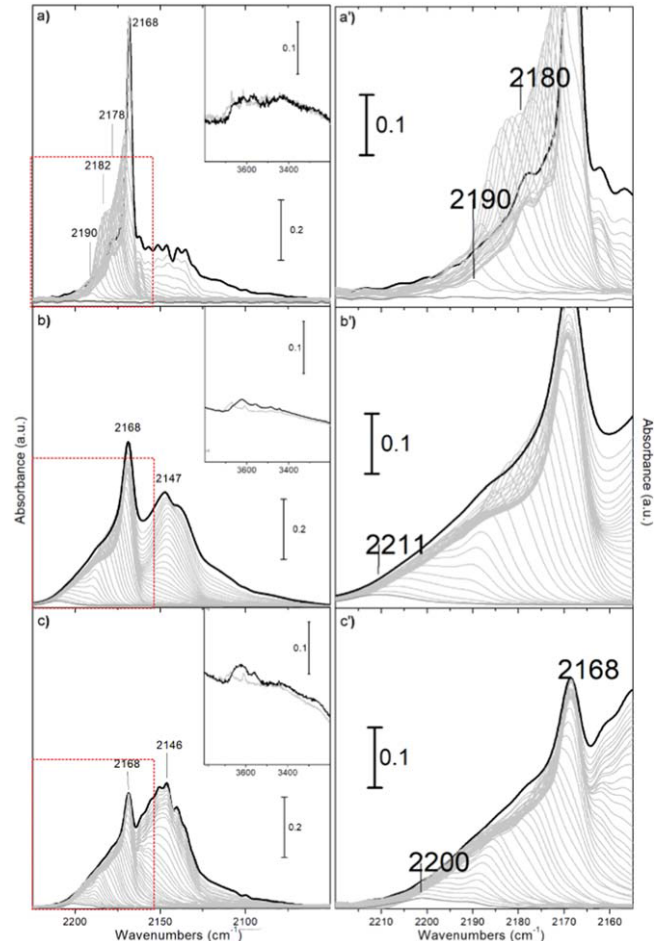
Samples	S_{BET}
ZnO-Ts as prepared	18
ZnO-Ts centrifuged @1000 rpm	23
ZnO-Ts centrifuged @2000 rpm	27
ZnO-Ts centrifuged @3000 rpm	30
ZnO powder (Kadox 25)	9

**Figure 5.** BET analysis of ZnO-Ts before centrifugation (1-curves), after centrifugation at 1000 rpm, 2000 rpm and 3000 rpm (2,3,4-curves, respectively): (a) N_2 -adsorption/desorption isotherms; (b) pore size distributions.

oxygen from air onto the surface [36]



This adsorption results in the capturing of electrons by the adsorbed oxygen, forming an ultra-thin electron-depletion layer on the surface of the UV sensor [36]. The current increase under UV illumination is related to the release of O_2 molecules which were adsorbed on the ZnO surface in the absence of UV light [37], because illumination with UV light exceeding the bandgap of ZnO electron–hole pairs are generated, O_2 molecules capture the hole and detach from the surface, while remaining electrons increase the conductivity.

**Figure 6.** FTIR spectra of CO adsorbed at 100 K on ZnO-Ts as obtained before centrifugation (a); ZnO-Ts after centrifugation at 1000 rpm (b); ZnO-Ts after centrifugation at 3000 rpm (c). Enlarged views of the 2210–2155 cm^{-1} range are shown in panels (a'), (b'), (c'), respectively. Insets in panel 6 (a), (b), (c) show the hydroxyl regions.

The I – V characteristics of ZnO showed the symmetric shape curves and orders of magnitude higher conduction values in the presence of UV illumination compared to measurement in dark conditions (figure 9(a)). The initial mixture of ZnO-Ts had the highest conductance of all in dark and UV conditions (figure 9(a)), which could be due to ZnO morphology, as this fraction contains the largest and the longest particles. However, the fraction of ZnO-Ts obtained at 1000 rpm possessed improved UV response properties compared to both the larger and smaller counterparts (figure 9(b)), moreover the photoresponse was repeatable

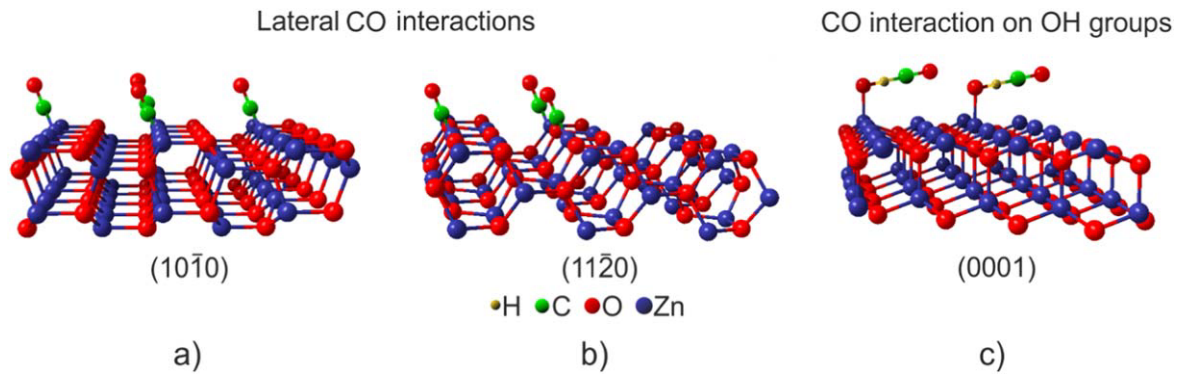


Figure 7. Model of CO lateral interactions on (a) $(10\bar{1}0)$ and (b) $(11\bar{2}0)$ prismatic surfaces; (c) model of CO interaction on hydroxyl groups adsorbed on (0001) basal surfaces.

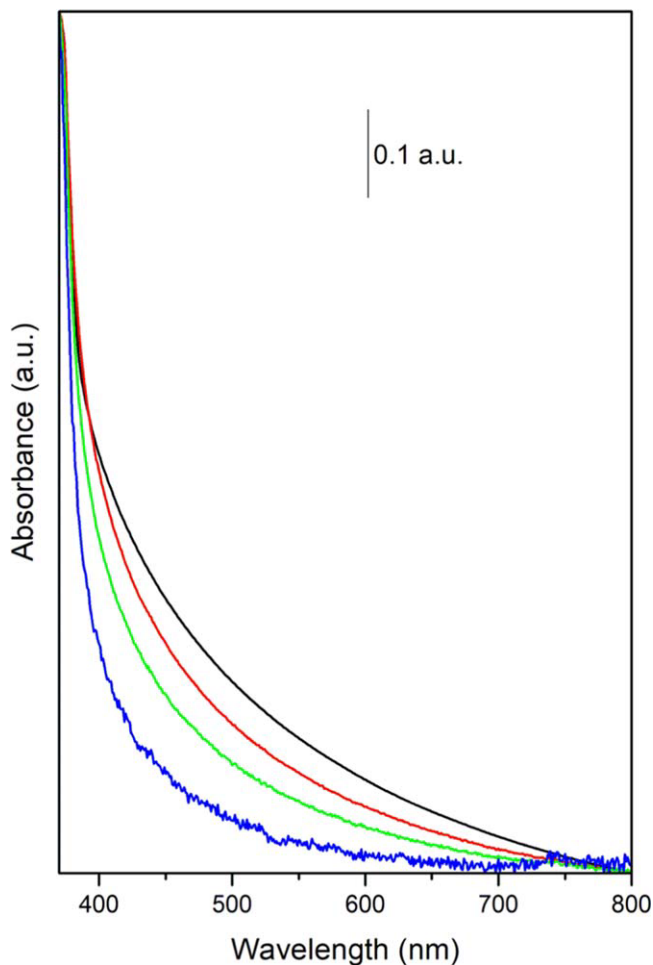


Figure 8. UV-vis spectra of ZnO-Ts as obtained after the synthesis procedure (black curve), after centrifugation at 1000 rpm (red curve), at 2000 rpm (green curve) and at 3000 rpm (blue curve), as collected from the supernatant fraction of the centrifuged solution.

(figure 9(c)). Commercial ZnO powder Kadox showed the lowest responsivity compared to (100) and (002) surfaces of ZnO-Ts synthesized in this work. Measured responsivity, which is defined as the ratio of output current to incident optical power is comparable to the other similar morphology ZnO nanoparticle (table 2), however the fraction of the

ZnO-Ts centrifuged at 1000 rpm showed order of. To explain the efficiency of different ZnO morphologies 3 different parameters can be considered: porosity, different facet activity, active diameter.

In chemoresistive sensors high porosity is directly influencing the sensitivity [35], however the process involves only the active surface of the sensor, which can be reached by gas and UV, therefore it is important that O_2 has the ability to penetrate the smallest pores [38]. From BET analysis (figure 5) we found the ZnO-Ts have similar porosities even at different centrifugation speeds, therefore such high difference in responsivity cannot be explained by solely small porosity changes. In case of Kadox, the porosity is 3 times lower than ZnO-Ts, therefore a negative influence on responsivity can be expected.

Various facets show different activity, i.e. photodegradation is facet dependent for ZnO [39] and also for other metal oxides [40]. In case of chemoresistive ZnO sensors Zn terminated (polar) surfaces have the highest chemisorption ability which leads to the highest sensitivity, demonstrating a 3-fold increased sensor response of nanodisc with (0001) polar facet compared to nanowires with predominant nonpolar facets [41]. However, the most of ZnO tetrapods surface is non-polar, which is connected to the growth of ZnO legs in c -axis orientation, leading to polar tip and all nonpolar side walls (basal and prismatic faces, as discussed in section 3.2). Different gas adsorption dynamics on basal and prismatic faces can be also noticed in FTIR measurements discussed in section 3.4 (figures 6 and 7), which might also indicate the possibility of different adsorption sites created. However, even if basal phases are prone to adsorb higher amount of gas, this still cannot explain the high response difference of smaller ZnO-Ts compared to larger (centrifuged at 3000 rpm and 1000 rpm, respectively), as both small and large tetrapods have similar basal to prismatic face ratio. Moreover, with random orientation of ZnO-Ts legs most of the leg-leg contacts are forming on the -polar surfaces, therefore percolation path does not involve polar tips as it is shown schematically in figure 10(b).

However, the most of ZnO tetrapods surface is non-polar, which the Debye length as an indicator of the electric field's

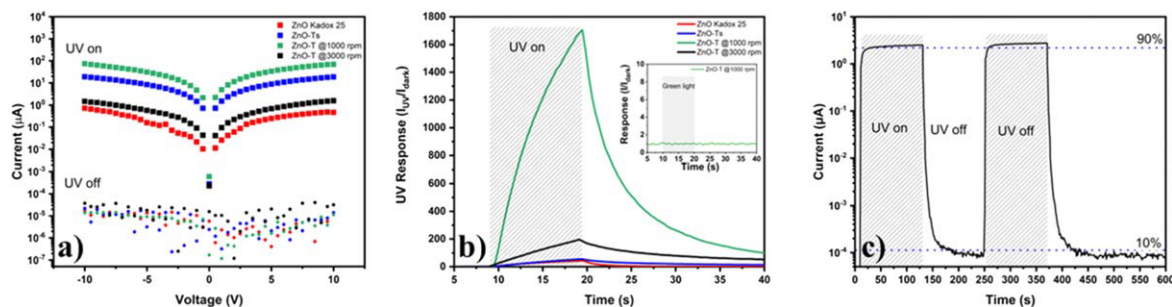


Figure 9. Photoresponse characteristics: current–voltage (I – V) curves recorded with and without UV irradiation (a); dynamic response of ZnO-Ts, compared to commercial ZnO powder (Kadox 25), inset shows no photoresponse of ZnO-Ts to green light; (b) repeatable dynamic response of ZnO-Ts centrifuged at 1000 rpm (c).

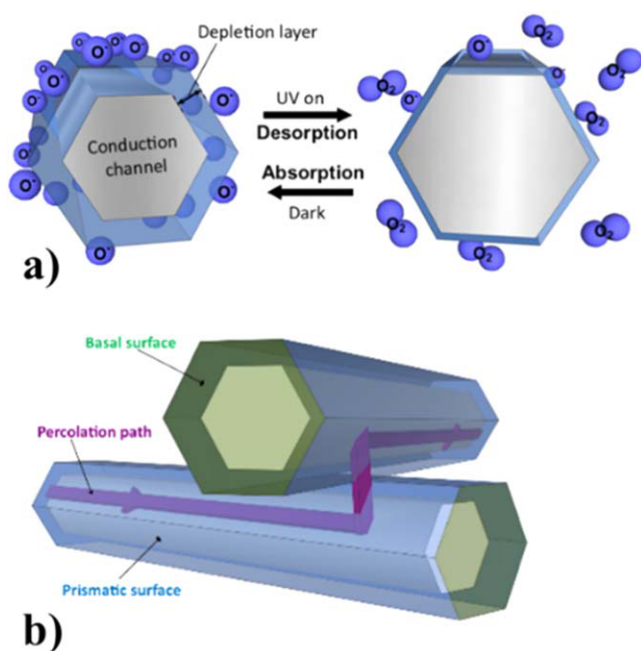


Figure 10. Photoresponse mechanism of chemoresistive ZnO sensors: depletion layer variation due to O_2 adsorption–desorption (a); percolation path through random nanowire–nanowire junction (b).

range within a substance, is critical to the efficiency of ZnO UV sensors [36, 42]. The sensor's sensitivity is influenced by the Debye length, which is directly related to the built-in electric field [37] that divides the electron–hole pairs. A higher sensitivity of ZnO UV sensors is the result of a stronger built-in electric field, which was influenced by morphology, doping level, and the Debye length [39]. With a Debye length of around 19 nm at room temperature [36], the best responsivity can be achieved for ZnO nanoparticles with diameters exceeding 38 nm. According to the XRD measurements (table 1) only the ZnO-Ts fraction, centrifuged at 3000 rpm has an average diameter smaller than double Debye length, which might hinder the responsivity, as the percolation path cannot spread through the channels which are fully depleted. On the other hand, ZnO-T fraction centrifuged at 1000 rpm has the average diameter larger than double Debye length and at the same time closest to its value,

which might influence the highest responsivity. In comparison as prepared ZnO-Ts fraction has the highest average diameter, but lower responsivity, indicating that the optimal ratio between the conduction channel and the depleted region is exceeded.

Compared to earlier works on nanomaterials-based UV sensors (table 1), our ZnO-T UV sensors, prepared in this work demonstrate good UV photoresponse properties, especially responsivity and photoresponse. Mishra *et al* [46] used ZnO-T network for UV sensing, demonstrating lower photoresponse but higher rise and decay times ($\tau_{\text{rise}} = 40$ ms and $\tau_{\text{decay}} = 50$ ms), which were 2 orders of magnitude lower than ours, which might be connected to their the longer interelectrode-gap used (100 μm). Grottrup *et al* [47] used hybrid ZnO tetrapod 3D networks, utilizing 48 times higher UV light intensity, however photoresponse for the ZnO-T:CuO (20:1) hybrid network was 21 times lower than our ZnO-T@3000, however their rise and decay times were also much lower. Postica *et al* [45] used a UV light intensity 32 times compared to our work, however the obtained photoresponse was ~ 10 times lower, demonstrating lower both rise and decay times. Similar results were demonstrated with other metal oxide nanowire-based UV sensors: SnO₂ nanowires [50] showed responsivity of 0.36 mA W^{-1} with a 0.7 rise time, whereas WO₃ nanowires [51] showed responsivity of 462.6 A W^{-1} with a 2.7 ms rise time.

ZnO-Ts investigated in this work showed similar response and decay times (table 3), which might indicate the similar response mechanism involved, however the enhanced responsivity was observed for the ZnO-Ts centrifuged at 1000 rpm. The discussed influence of porosity and different facet ratio could not explain such a high difference in responsivity of ZnO-T centrifuged at 1000 rpm: responsivity was 4-fold higher than as prepared ZnO-Ts and even 2 orders of magnitude higher than ZnO-Ts centrifuged at 3000 rpm. The ZnO-T diameter proximity to Debye length shows the most influence on the responsivity, as the average diameters were largest for the initial ZnO-Ts and smallest for the fraction centrifuged at 3000 rpm, with the ZnO-Ts fraction centrifuged at 1000 rpm giving the average diameter closest to double Debye length, which explains the highest responsivity.

Table 3. Responsivity of ZnO UV photodetectors.

Photodetector	Bias (V)	λ (nm)	Intensity of light (mW/cm ²)	Responsivity (A/W)	I_{UV}/I_{Dark} (a. u.)	τ_{rise} (s)	τ_{decay} (s)	References
Kadox	-5	365	0.31	$5.10 \cdot 10^{-1}$	$1.17 \cdot 10^4$	8.68	19.93	This Work
ZnO-T	-5	365	0.31	$2.71 \cdot 10^2$	$2.66 \cdot 10^6$	8.32	19.11	This Work
ZnO-T@1000	-5	365	0.31	$9.98 \cdot 10^2$	$3.39 \cdot 10^6$	8.81	19.24	This Work
ZnO-T@3000	-5	365	0.31	$1.86 \cdot 10^0$	$3.22 \cdot 10^4$	8.45	19.03	This Work
ZnO nanowires	5	365	1.50	N/A	$2.32 \cdot 10^3$	3.90	2.60	[43]
ZnO seed layer	5	365	1.50	$8.00 \cdot 10^{-1}$	$7.68 \cdot 10^3$	0.90	1.30	[44]
ZnO-T	5	365	10	$5.20 \cdot 10^{-2}$	$3.10 \cdot 10^3$	~ 1	~ 1	[45]
ZnO nanorods (Ga-doped)	1	360	N/A	$0.46 \cdot 10^{-2}$	$5.76 \cdot 10^2$	89	106	[42]
ZnO-T Network	N/A	365	N/A	N/A	$5.84 \cdot 10^2$	0.04	0.05	[46]
ZnO-T:CuO (20:1) hybrid network	N/A	365	15	N/A	$1.50 \cdot 10^3$	0.03	0.045	[46, 47]
Single ZnO-T:Al MW	5	365	15	N/A	5.5	0.23	0.39	[47]
Single ZnO nanotetrapod-based sensor	2	325	30	N/A	1.7	2.20	6.00	[23]
ZnO:Ga (3%) film based UV detector	5	385	5	0.38	N/A	1	3.2	[48]
ZnO-NRs	-3	390	0.57	2.19	N/A	0.49	1.14	[49]

4. Conclusions

In this study ZnO-Ts (ZnO tetrapods) were synthesized and divided into three fractions by centrifugation at different speeds (as prepared, centrifuged at 1000 rpm and 3000 rpm). Each fraction exhibited specific morphology, which was characterized by SEM, HR-TEM, XRD, and BET analyses, FTIR and UV-vis spectroscopies. To investigate the ZnO-T photoresponse dependence on morphology UV sensing experiments were performed. Our findings revealed that the ZnO-T diameter proximity to double Debye length (38 nm) had the most significant impact on photoresponse, whereas porosity and surface facet orientation had much lower influence. Responsivity of ZnO-T centrifuged at 1000 rpm: responsivity was four times higher than as prepared ZnO-Ts and even 2 orders of magnitude higher than ZnO-Ts centrifuged at 3000 rpm. Optimized ZnO-Ts also showed 3 orders of magnitude superior responsivity to commercial ZnO nanopowder (Kadox), and to other nanostructures reported earlier. Our work presents a practical approach for considerable UV photoresponse optimization, and demonstrates the importance of the morphology control, specifically the diameter's influence, in enhancing photoresponse in chemoresistive photodetectors based on one-dimensional materials.

Acknowledgments

This work was funded from the European Regional Development Fund (Project No. 01.2.2-LMT-K-718-02-0011) under a grant agreement with the Research Council of Lithuania (LMTLT). FC, SC, CB, DS, and GV acknowledge support from the Project CH4.0 under the MUR programme 'Departments of Excellence 2023-2027' (CUP: D13C22003520001).

Data availability statement

All data that support the findings of this study are included within the article (and any supplementary files).

ORCID iDs

Mindaugas Ilickas  <https://orcid.org/0000-0003-0682-0133>
 Federico Cesano  <https://orcid.org/0000-0002-4056-4738>
 Sara Cravanzola  <https://orcid.org/0000-0003-0400-4335>
 Domenica Scarano  <https://orcid.org/0000-0002-3686-3436>
 Guido Viscardi  <https://orcid.org/0000-0002-9387-2849>
 Simas Rackauskas  <https://orcid.org/0000-0002-8964-5299>

References

- [1] Gleiter H 2000 Nanostructured materials: basic concepts and microstructure *Acta Mater.* **48** 1-29
- [2] Scarano D, Bertarione S, Cesano F, Spoto G and Zecchina A 2004 Imaging polycrystalline and smoke MgO surfaces with atomic force microscopy: a case study of high resolution image on a polycrystalline oxide *Surf. Sci.* **570** 155-66
- [3] Capek I 2006 Nanotechnology and nanomaterials *Nanocomposite Structures and Dispersions, Science and Nanotechnology—Fundamental Principles and Colloidal Particles* (Elsevier) Amsterdam Studies in Interface Science Volume 23 of Studies in interface science series pp 1-69
- [4] Arbiol J, de la Mata M, Eickhoff M and Morral A F I 2013 Bandgap engineering in a nanowire: self-assembled 0, 1 and 2D quantum structures *Mater. Today* **16** 213-9
- [5] Jariwala D, Marks T and Hersam M 2017 Mixed-dimensional van der Waals heterostructures *Nat. Mater.* **16** 170-81
- [6] Cravanzola S, Cesano F, Magnacca G, Zecchina A and Scarano D 2016 Designing rGO/MoS₂ hybrid nanostructures for photocatalytic applications *RSC Adv.* **6** 59001-8
- [7] Chen W-C, Zhu Z-L and Lee C-S 2018 Organic light-emitting diodes based on imidazole semiconductors *Adv. Opt. Mater.* **6** 1800258
- [8] Kory M J, Wörle M, Weber T, Payamyar P, van de Poll S W, Dshemuchadse J, Trapp N and Schlüter A D 2014 Gram-scale synthesis of two-dimensional polymer crystals and their structure analysis by x-ray diffraction *Nat. Chem.* **6** 779-84
- [9] Kissel P, Erni R, Schweizer W B, Rossell M D, King B T, Bauer T, Göttinger S, Schlüter A D and Sakamoto J 2012 A two-dimensional polymer prepared by organic synthesis *Nat. Chem.* **4** 287-91
- [10] Zhang N, Wang T, Wu X, Jiang C, Zhang T, Jin B, Ji H, Bai W and Bai R 2017 From 1D polymers to 2D polymers: preparation of free-standing single-monomer-thick two-dimensional conjugated polymers in WATER *ACS Nano* **11** 7223-9
- [11] Cesano F and Scarano D 2018 Graphene and other 2D layered hybrid nanomaterial-based films: synthesis, properties, and applications *Coatings* **8** 419
- [12] Toh C-T et al 2020 Synthesis and properties of free-standing monolayer amorphous carbon *Nature* **577** 199-203
- [13] Rackauskas S, Klimova O, Jiang H, Nikitenko A, Chermenko K A, Shandakov S D, Kauppinen E I, Tolochko O V and Nasibulin A G 2015 A novel method for continuous synthesis of ZnO tetrapods *J. Phys. Chem.C* **119** 16366-73
- [14] Zhao Y, Liu N, Zhou S and Zhao J 2019 Two-dimensional ZnO for the selective photoreduction of CO₂ *J. Mater. Chem.A* **7** 16294-303
- [15] Scarano D, Bertarione S, Cesano F, Vitillo J G and Zecchina A 2006 Plate-like zinc oxide microcrystals: synthesis and characterization of a material active toward hydrogen adsorption *Catal. Today* **116** 433-8
- [16] Alammari T and Mudring A-V 2011 Sonochemical synthesis of 0D, 1D, and 2D zinc oxide nanostructures in ionic liquids and their photocatalytic activity *ChemSusChem* **4** 1796-804
- [17] Lee Y B, Kim S K, Lim Y R, Jeon I S, Song W, Myung S, Lee S S, Lim J and An K-S 2017 Dimensional-hybrid structures of 2D materials with ZnO nanostructures via pH-mediated hydrothermal growth for flexible UV photodetectors *ACS Appl. Mater. Interfaces* **9** 15031-7
- [18] Scarano D, Cesano F, Bertarione S and Zecchina A 2018 Zinc oxide nanostructures: from chestnut husk-like structures to hollow nanocages, synthesis and structure *Crystals (Basel)* **8** 153
- [19] Modi G 2015 Zinc oxide tetrapod: a morphology with multifunctional applications *Adv. Nat. Sci.: Nanosci. Nanotechnol.* **6** 033002
- [20] Mishra Y K and Adelung R 2018 ZnO tetrapod materials for functional applications *Mater. Today* **21** 631-51
- [21] Sulciute A, Nishimura K, Gilshtein E, Cesano F, Viscardi G, Nasibulin A G, Ohno Y and Rackauskas S 2021 ZnO

- nanostructures application in electrochemistry: influence of morphology *J. Phys. Chem.C* **125** 1472–82
- [22] Ilickas M, Marčinskis M, Peckus D, Mardosaitė R, Abakevičienė B, Tamulevičius T and Račkauskas S 2023 ZnO UV sensor photoresponse enhancement by coating method optimization *J. Photochem. Photobiol.* **14** 100171
- [23] Wang W, Qi J, Wang Q, Huang Y, Liao Q and Zhang Y 2013 Single ZnO nanotetrapod-based sensors for monitoring localized UV irradiation *Nanoscale* **5** 5981
- [24] Muñoz E, Monroy E, Pau J L, Calle F, Omnès F and Gibart P 2001 III nitrides and UV detection *J. Phys. Condens. Matter* **13** 7115–37
- [25] Liu K, Sakurai M and Aono M 2010 ZnO-based ultraviolet photodetectors *Sensors* **10** 8604–34
- [26] Araki H, Yang W, Hu Q, Suzuki H and Noda T 2005 Fabrication and fracture toughness of SiC nanowires/ Tyranno-SA/SiC composite *Novel Materials Processing by Advanced Electromagnetic Energy Sources* (Amsterdam: Elsevier) 369–72
- [27] Kearns J K 2019 Silicon single crystals *Single Crystals of Electronic Materials* (Elsevier) pp 5–56
- [28] Bare S R and Somorjai G A 2003 Surface chemistry *Encyclopedia of Physical Science and Technology* (Elsevier) pp 373–421
- [29] Kraynik A M, Reinelt D A and Loewenberg M 2001 Foams, microrheology *Encyclopedia of Materials: Science and Technology* (Elsevier) p 3221–6
- [30] Tamulevičius T, Laurikėnas P, Juodėnas M, Mardosaitė R, Abakevičienė B, Pereyra C J and Račkauskas S 2023 Antireflection coatings based on randomly oriented ZnO nanowires *Sol. RRL* **7** 2201056
- [31] Scarano D, Spoto G, Bordiga S, Zecchina A and Lamberti C 1992 Lateral interactions in CO adlayers on prismatic ZnO faces: a FTIR and HRTEM study *Surf. Sci.* **276** 281–98
- [32] Zak A K, Abrishami M E, Majid W H A, Yousefi R and Hosseini S M 2011 Effects of annealing temperature on some structural and optical properties of ZnO nanoparticles prepared by a modified sol–gel combustion method *Ceram. Int.* **37** 393–8
- [33] Zhao Z W, Tay B K, Chen J S, Hu J F, Sun X W and Tan S T 2005 Optical properties of nanocluster-assembled ZnO thin films by nanocluster-beam deposition *Appl. Phys. Lett.* **87** 251912
- [34] Carrada M, Wellner A, Paillard V, Bonafos C, Coffin H and Claverie A 2005 Photoluminescence of Si nanocrystal memory devices obtained by ion beam synthesis *Appl. Phys. Lett.* **87** 251911
- [35] Rackauskas S, Barbero N, Barolo C and Viscardi G 2017 ZnO Nanowire application in chemoresistive sensing: a review *Nanomaterials* **7** 381
- [36] Lee J-H, Kim J-Y, Kim J-H and Kim S 2019 Enhanced hydrogen detection in ppb-level by electrospun SnO₂-loaded ZnO nanofibers *Sensors* **19** 726
- [37] Park J, Lee J, Noh Y, Shin K-H and Lee D 2016 Flexible ultraviolet photodetectors with ZnO nanowire networks fabricated by large area controlled roll-to-roll processing *J. Mater. Chem.C* **4** 7948–58
- [38] Nasiri N, Bo R, Wang F, Fu L and Tricoli A 2015 Ultraporous electron-depleted ZnO nanoparticle networks for highly sensitive portable visible-blind UV photodetectors *Adv. Mater.* **27** 4336–43
- [39] Chang J and Waclawik E R 2012 Facet-controlled self-assembly of ZnO nanocrystals by non-hydrolytic aminolysis and their photodegradation activities *CrystEngComm* **14** 4041
- [40] Gao X and Zhang T 2018 An overview: facet-dependent metal oxide semiconductor gas sensors *Sensors ActuatorsB* **277** 604–33
- [41] Alenezi M R, Alshammari A S, Jayawardena K D G I, Beliatas M J, Henley S J and Silva S R P 2013 Role of the exposed polar facets in the performance of thermally and UV activated ZnO nanostructured gas sensors *J. Phys. Chem. C* **117** 17850–8
- [42] Young S-J et al 2020 Flexible ultraviolet photodetectors based on one-dimensional gallium-doped zinc oxide nanostructures *ACS Appl. Electron. Mater.* **2** 3522–9
- [43] Alsultany F H, Hassan Z and Ahmed N M 2016 A high-sensitivity, fast-response, rapid-recovery UV photodetector fabricated based on catalyst-free growth of ZnO nanowire networks on glass substrate *Opt. Mater.* **60** 30–7
- [44] Alsultany F H, Hassan Z, Ahmed N M, Elafadill N G and Abd H R 2018 Effects of ZnO seed layer thickness on catalyst-free growth of ZnO nanostructures for enhanced UV photoresponse *Opt. Laser Technol.* **98** 344–53
- [45] Postica V, Paulowicz I, Lupan O, Schütt F, Wolff N, Cojocaru A, Mishra Y K, Kienle L and Adelung R 2019 The effect of morphology and functionalization on UV detection properties of ZnO networked tetrapods and single nanowires *Vacuum* **166** 393–8
- [46] Mishra Y K et al 2015 Direct growth of freestanding ZnO tetrapod networks for multifunctional applications in photocatalysis, UV photodetection, and gas sensing *ACS Appl. Mater. Interfaces* **7** 14303–16
- [47] Gröttrup J, Postica V, Smazna D, Hoppe M, Kaidas V, Mishra Y K, Lupan O and Adelung R 2017 UV detection properties of hybrid ZnO tetrapod 3D networks *Vacuum* **146** 492–500
- [48] Kumar K D A, Mele P, Murahari P, Abdeltawab A A, Mohammady S Z, Ubaidullah M, Samdani M S and AlFaify S 2022 Enhancement of performance of Ga incorporated ZnO UV photodetectors prepared by simplified two step chemical solution process *Sensors ActuatorsA* **333** 113217
- [49] Abdulrahman A F, Abd-Alghafour N M and Almessiere M A 2023 A high responsivity, fast response time of ZnO nanorods UV photodetector with annealing time process *Opt. Mater.* **141** 113869
- [50] Chetri P and Dhar J C 2019 Self-powered UV detection using SnO₂ nanowire arrays with Au Schottky contact *Mater. Sci. Semicond. Process.* **100** 123–9
- [51] Singh A K, Chetri P and Dhar J C 2023 Interdigitated electrodes connected WO₃ nanowire arrays for high performance UV photodetection *Mater. Lett.* **333** 133692